# A Dual Band Focal Plane Array of Kinetic Inductance Bolometers Based on Frequency Selective Absorbers

Dabironezare, Shahab Oddin; Hassel, Juha; Gandini, Erio; Grönberg, Leif; Sipola, Hannu; Vesterinen, Visa; Llombart, Nuria

**DOI**
10.1109/TTHZ.2018.2873973

**Publication date**
2018

**Document Version**
Accepted author manuscript

**Published in**
IEEE Transactions on Terahertz Science and Technology

# A Dual Band Focal Plane Array of Kinetic Inductance Bolometers Based on Frequency Selective Absorbers

Shahab Oddin Dabironezare[1], *Student Member, IEEE,* Juha Hassel[2], Erio Gandini[1], Leif Grönberg[2], Hannu Sipola[2], Visa Vesterinen[2], Nuria Llombart[1], *Senior Member, IEEE*
[1] Terahertz Sensing Group, Delft University of Technology, Delft, the Netherlands
[2] VTT Technical Research Center of Finland, Helsinki, Finland

***Abstract*— Passive imaging cameras at sub-millimeter wavelengths with large format focal plane arrays are being developed as the next generation of security screening systems. In this contribution, a dual-band focal plane array (FPA) for security imagers at submillimeter wave frequencies is presented. The detectors are based on bolometric superconducting kinetic inductance resonators, which allows the development of large FPAs at medium cooled temperatures. Two frequency selective absorber (FSA) sets coupled to superconductive resonator lines are designed to implement a dual color security imager. The performance of the dual band imager is evaluated using spectral analysis approach that combines Fourier optics with a Floquet mode field representation. The geometry of the unit cells is based on a Jerusalem cross configuration and the designed FSAs show a stable angular response and a rejection 1 to 3 of the undesired bandwidth. The detectors in the dual band FPA are distributed over a hexagonal grid to maximize their physical size and then improve their sensitivity. The effective point spread function of the imager coupled to a black body point source over a wide frequency band (1:6) was demonstrated experimentally with excellent agreement to the one estimated by using the proposed spectral technique.**

**Index Terms— Sub-mm wavelengths, focal plane array, frequency selective absorber, incoherent source.**

## I. Introduction

The next generation of THz imagers for stand-off detection of concealed weapons, [1]–[4], will require the acquisition of images as large as a human body, over 100000 pixels, at quasi-video rate, higher than 10 Hz. The architecture of such imagers is typically composed of a quasi-optical system, a focal plane array (FPA) and a mechanical scanner. A FPA with a large number of elements would dramatically reduce the need for a fast-mechanical repointing of the optics, and, consequently, allows a much longer integration time for the detectors (comparable in this case to the frame rate), thus relaxing the required detector sensitivity. However, the design of large FPAs at sub-millimeter wavelengths remains a significant challenge and, in practice, the state-of-the-art passive imagers are implemented with a limited number of detectors ($< 200$) [2], [4]–[6].

Promising solutions for development of sub-millimeter wavelength FPAs in the order of several thousands of detectors are based on kinetic inductance detectors (KIDs) [7]–[9]. The latter are incoherent superconductor based detectors and many of them can be coupled to a single low-frequency read-out line, decreasing significantly the complexity of large FPA architectures. The coupling of the KIDs to the read-out line is based on low frequency superconductive resonators with high quality factor. The radiation at submillimeter wavelengths can be absorbed either via antennas coupled to resistive transmission lines [8] or bare absorbers [10]. The power absorption corresponds to a shift of the resonant frequency and a decrease of the quality factor.

KIDs can operate in two different regions. The non-equilibrium mode relies on the finite lifetime of the quasiparticle excitations [8]. Here we concentrate on the kinetic inductance bolometer (KIB) mode in which the superconductor is in a local thermal equilibrium with its surroundings, and the detection is based on the temperature dependence of the inductance [11].

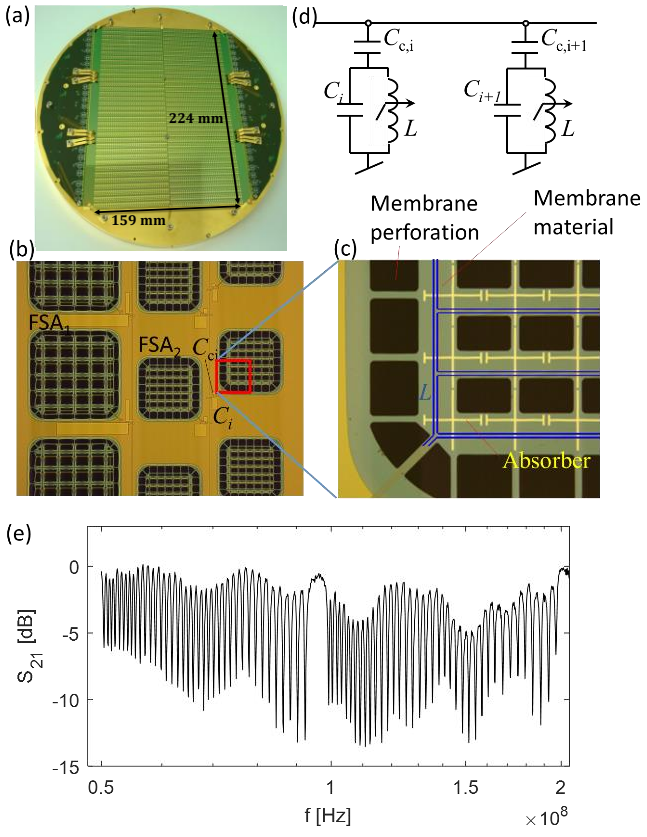


Fig. 1. (a) The dual band FPA with 8208 kinetic inductance bolometers. (b) A microphotograph illustrating the two FSA sets. (c) A zoom-up showing a piece of detector membrane and the structures on it. The kinetic inductance thermometer *L* is emphasized in blue for clarity. (d) Electrical equivalent circuit of a piece of multiplexed readout line. (e) The readout band transmission spectrum within a readout channel with each spike corresponding to an individual readout frequency of a detector.

The noise equivalent power (NEP) of KIDs operating in non-equilibrium mode is in the order of $10^{-20}$ W/Hz$^{1/2}$ [8] for operation temperature below 1 K. This configuration was used for security imagers in [5]. The main drawback of this solution is the high cost of the required top-performance cryostat.

In the thermal region, KIBs measure the temperature change of the THz radiation absorbed over a thermally isolated volume. Similar to non-equilibrium mode, the variation in the inductance of the structure can be read-out via superconductive resonators. However, in this region, the requirement for the operating temperature is relaxed to about 5 to 10 K, allowing the use of low-cost cryogenic coolers. The NEP of these detectors is in the order of $10^{-15}$ W/Hz$^{1/2}$ [11], higher than the non-equilibrium mode, but sufficient for security applications. Therefore, KIBs provide the possibility of having large FPAs with medium cooled temperature and a reasonable cost for passive imaging [11].

Exploiting this technology, in this work, a FPA suited for future security applications is designed as shown in Fig. 1(a). The outer diameter of the FPA has been set to $\emptyset = 24\ cm$, corresponding to the maximum useful window of the cryostat. The basic structure of the focal plane and the detectors is depicted in the microphotographs of Figs. 1(b) and (c). The total number of the detectors is 8208, organized on six detector tiles with 80 mm X 75 mm active area consisting of 1368 detectors. The thermal isolation is obtained via through-wafer released membrane which is perforated to optimize the thermal coupling to the substrate, and to minimize the heat capacity. For readout, the thermometer is tuned into an individual RF readout frequency with an off-membrane tuning capacitor $C_i$ and matched to a 50 Ω readout line with a coupling capacitor $C_{c,i}$ as schematically illustrated in Fig. 1(d). Here $i$ refers to the detector index within a readout channel consisting of 114 detectors per channel in this case. The total number of readout channels is 72. The readout band transmission within one readout channel is plotted in Fig. 1(e). Similar data was acquired from 15 readout channels indicating good detector yield ($> 95\%$) in line with the data of [11]. Moreover, in [12], concealed object detection has been demonstrated with the imaging system which is described in this work, i.e. the same optical system together with the designed dual band FPA.

Security applications demand high probability of detection, which can be achieved by using passive images taken at different frequency bands [6], i.e. multi-band images. To this end, we propose here to modify the absorber design in [9] to be frequency selective [13] around specific frequency bands. The FPA will then consist of frequency selective absorbers (FSAs) for the lower bandwidth centered at 250 GHz; interleaved with the ones for the higher bandwidth centered at 500 GHz; these detectors are referred to as $FSA_1$ and $FSA_2$, respectively, in Fig, 1(b). The proposed architecture can be operated in combination with a linear scanner to generate fully sampled images in the two bands. Each FSA detector set has been designed to absorb in its corresponding frequency band of operation and reject the radiation from the other band with a factor of 1 to 3. The use of a single frequency selective layer has been chosen as a compromise between the cost and the rejection factor. The quasi-optical system of the imager is a dual-lens architecture described in [14], which allows full body imaging. The f-number, $f_{\#}$, (ratio between the focal distance and diameter of the optics), is set to 2. Obtaining a two-dimensional image of the full human body is required from the application point of view. To achieve this requirement, a sparse two-dimensional absorber-based array is placed at the focal plane of the dual lens system. By combining this configuration with a one-dimensional mechanical scanner, the FoV is fully imaged in two dimensions.

In order to analyze the performance of an imager based on a FPA made of bare absorbers, the spectral Fourier optics (FO) technique described in [15] is used. This technique couples the spectrum of the optical system with a Floquet mode representation in the surrounding of the periodic absorber. This technique provides an accurate methodology to derive the point spread function (PSF) and efficiency of the imager to monochromatic point sources. The effective PSF of the imager coupled to a black body point source over a wide frequency band (1:6) was estimated theoretically and demonstrated experimentally. Finally, the performance of the imager coupled to a distributed incoherent source in terms of the sensitivity is evaluated.

The paper is structured as follows. Section II describes the design of the FSAs for the two operational bandwidths. The architecture of the dual-band focal plane array is discussed in Sec. III. In Section IV, the experimental validation of the performance of the imager in terms of the effective PSF is presented. Concluding remarks are reported in Sec. V.

## II. FSA Based KIBs

In this section, the geometry of the proposed detectors is presented and analyzed. The selected architecture and the design considerations used to optimize the frequency, angular and polarization responses are discussed. Moreover, the optimization of the FSA including the KIB resonator lines along with its performance is reported.

### *A. Design Considerations*

The geometry of the KIBs is introduced in [11] is shown in the inset of Fig. 2. The thermal confinement is achieved by placing the absorber and kinetic inductance thermometer on a 200 nm thick SiN membrane. The on-membrane structure is composed of two layers: a resistive mesh grid with a surface resistance of $R_s = 5\ \Omega/\square$, and a superconducting meander strip acting as the thermometer below the grid. The superconductor material is NbN with the nominal critical temperature of 11 K as estimated from the calibration measurements of films deposited with similar parameters. The surface impedance of the superconductive material, in the submillimeter wavelengths, is shown in Fig. 2 as estimated from the theory of Mattis and Bardeen [16][16]. The layers are separated by a thin $SiO_2$ layer with the thickness of 150 nm and dielectric constant $\varepsilon_r \simeq 5$. The mesh grid absorbs the incoming radiation, and heats the elements on the membrane, which in the operating temperature range of $5 - 10$ K are essentially in thermal equilibrium. The thermal conductivities from the membrane to the substrate of the membranes are estimated from the geometry and experimentally recorded material parameters in [9] to be 190 nW/K and 140 nW/K for the $FSA_1$ and $FSA_2$ detectors, respectively. The temperature dependence of the

superconducting kinetic inductance is then used to read-out the temperature change.

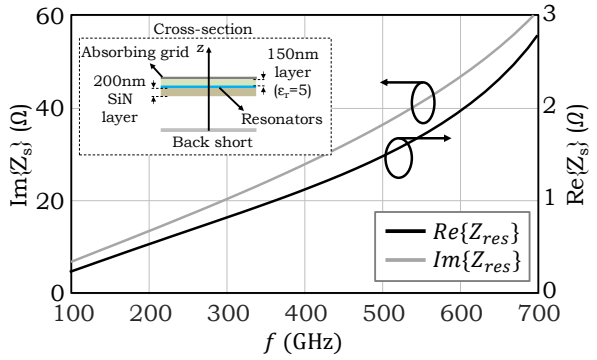


Fig. 2. The surface impedance of the proposed superconductive resonator. Inset shows the cross-section of the detectors where the resistive layer, the resonator lines, and thin dielectric membrane are indicated by the colors grey, blue, and green, respectively.

In this paper, the goal is to design the detector's geometry as two different FSA layouts each with a limited bandwidth around 250 GHz and 500 GHz, respectively, with a nearly flat angular response up to 30°. This requirement is due to the geometrical size of the FPA with respect to the dual lens system. At the worst case, i.e. for detectors at the edge of the FPA, the rays arriving from the dual lens system illuminate the detector with a maximum incident angle of 30°.

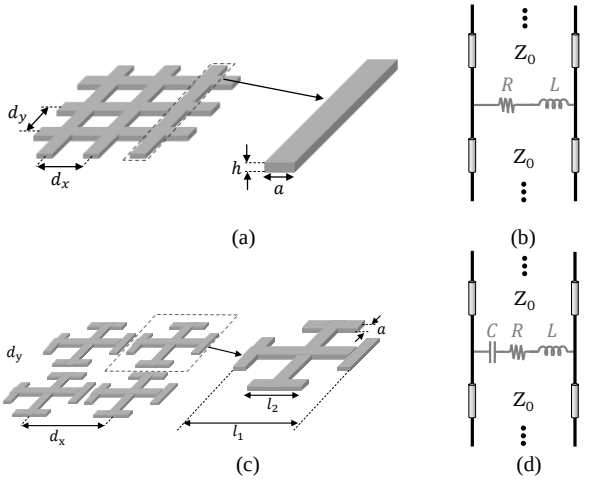


Fig. 3. Geometry (a) and equivalent circuit representation (b) of a resistive squared mesh. Geometry (c) and equivalent circuit representation (d) of a free-standing FSA.

For broadside plane wave incidence, a resistive square mesh, Fig. 3(a), can be modelled using an equivalent circuit model, Fig. 3(b), with a resistance and an inductance in parallel to a transmission line representing the fundamental Floquet modes. The lumped elements values can be calculated analytically [17], and are reported in Table 1, where $R$, $L$ and $C$ parameters represent the lumped resistance, inductance and capacitance, respectively. In order to introduce a frequency selectivity to the resistive layer, the mesh grid can be loaded with a distributed capacitance using the geometry of Fig. 3(c), typically referred to as a Jerusalem Cross (JC) [18]. The corresponding equivalent circuit is shown in Fig. 3(d), and it

TABLE 1
THE LUMPED ELEMENTS OF THE CIRCUIT MODEL

| Parameter | Mesh Grid | JC $FSA_1$ | JC $FSA_2$ |
|---|---|---|---|
| $R$ | 417 Ω | 420 Ω | 270 Ω |
| $L$ | $1.015 \times 10^{-10}\ H$ | $2.45 \times 10^{-10}\ H$ | $1.07 \times 10^{-10}\ H$ |
| $C$ | – | $16.5 \times 10^{-16}\ F$ | $6.25 \times 10^{-16}\ F$ |

presents an additional capacitance compared to the mesh grid, that allows a resonant behavior. The geometrical parameters of the designed sets of FSAs are reported in Table 2 (columns 2 and 4), where $\lambda_1$ and $\lambda_2$ are the wavelengths at 250 GHz and 500 GHz, respectively, whereas the corresponding lumped components, derived using CST MWS [19] simulation, are listed in Table 1. As shown in Fig. 4(a) (solid lines), the FSAs introduce a frequency selectivity not present in the original mesh grid.

The absorption rate and out of band rejection of a free-standing resistive layer can be improved by using a back short. The use of a quarter wavelength back short for the $FSA_1$ will introduce a significant rejection in the 500 GHz band. The $FSA_2$ is instead designed with a much closer back short, to short circuit the lower part of the frequency band. The capacitive behavior in the $FSA_2$ compensates the inductance introduced by the back short, allowing a reasonable impedance match to the free space impedance. The back short distance, $h_{bs}$, for the two FSA sets are reported in Table 2, and the described frequency response is shown in Fig. 4(b). The frequency selectivity could be further enhanced if the detectors were fabricated using a multi-layer periodic structure, similar to [20] and. However, one should take into account that in this work a reflect/absorb frequency selective structure is desired instead of a transmit/absorb one.

### *B. Proposed Unit Cell Implementation*

The KIB detection mechanism requires additional superconductive thermometer lines underneath the FSA separated by a dielectric membrane as mentioned in Sec. II.A. These superconductive lines can be modeled, as two thin horizontal strip lines with the sheet impedance as estimated from the theory of Mattis and Bardeen [16], as shown in Fig. 2. Due to the presence of the superconducting lines, the absorption rate of the FSAs, in terms of frequency and polarization response, is significantly altered. These effects, however, can be compensated for by modifying the geometry of the JC FSAs differently for vertical and horizontal polarizations. The proposed FSA unit cells combined with the resonators are shown in Fig. 5, and their geometrical parameters reported in Table 2 (columns 3 and 5). In Fig. 6, the simulated absorption rates for both optimized FSA sets are shown. The frequency variation is comparable to the one of the free-standing design. Moreover, no significant variation was observed for incidence angles up to 30° for both polarizations.

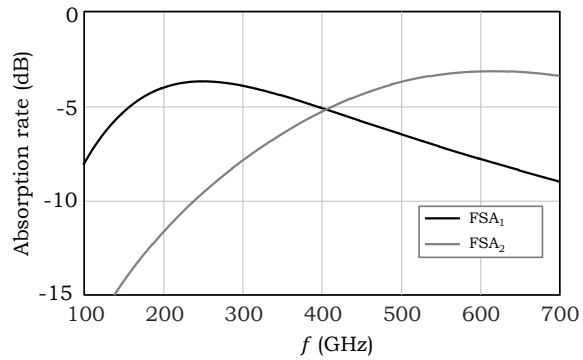


(a)

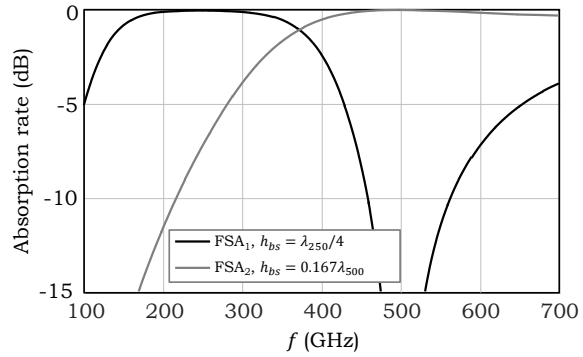


(b)

Fig. 4. The absorption rate, simulated with CST MWS, of a continuous strip line compared to two free-standing FSAs under a broadside plane wave incident: (a) without, and (b) with the back short layer.

### C. Proposed Unit Cell Implementation

The KIB detection mechanism requires additional superconductive thermometer lines underneath the FSA separated by a dielectric membrane as mentioned in Sec. II.A. These superconductive lines can be modeled, as two thin horizontal strip lines with the sheet impedance as estimated from the theory of Mattis and Bardeen [16], as shown in Fig. 2. Due to the presence of the superconducting lines, the absorption rate of the FSAs, in terms of frequency and polarization response, is significantly altered. These effects, however, can be compensated for by modifying the geometry of the JC FSAs differently for vertical and horizontal polarizations. The proposed FSA unit cells combined with the resonators are shown in Fig. 5, and their geometrical parameters reported in Table 2 (columns 3 and 5). In Fig. 6, the simulated absorption rates for both optimized FSA sets are shown. The frequency variation is comparable to the one of the free-standing design. Moreover, no significant variation was observed for incidence angles up to 30° for both polarizations.

TABLE 2
DESIGN PARAMETERS OF THE FSAS

| Parameter | Free-standing FSA$_1$ | FSA$_1$ + resonator | Free-standing FSA$_2$ | FSA$_2$ + resonator |
|---|---|---|---|---|
| $a$ | $0.003\lambda_1$ | $0.005\lambda_1$ | $0.005\lambda_2$ | $0.008\lambda_2$ |
| $l_1$ | $0.241\lambda_1$ | $0.238\lambda_1$ | $0.242\lambda_2$ | $0.237\lambda_2$ |
| $l_2$ | $0.108\lambda_1$ | $0.042\lambda_1$ | $0.042\lambda_2$ | $0.043\lambda_2$ |
| $l_3$ | – | $0.033\lambda_1$ | – | $0.243\lambda_2$ |
| $h_{bs}$ | $0.250\lambda_1$ | $0.250\lambda_1$ | $0.167\lambda_2$ | $0.167\lambda_2$ |
| $d$ | $0.250\lambda_1$ | $0.250\lambda_1$ | $0.250\lambda_2$ | $0.250\lambda_2$ |
| $a_{res}$ | – | $0.003\lambda_1$ | – | $0.007\lambda_2$ |
| $d_{res}$ | – | $0.071\lambda_1$ | – | $0.063\lambda_2$ |
| $\Delta_{res}$ | – | $0.004\lambda_1$ | – | $0.008\lambda_2$ |

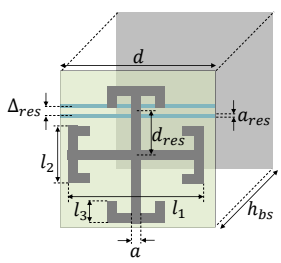


(a)

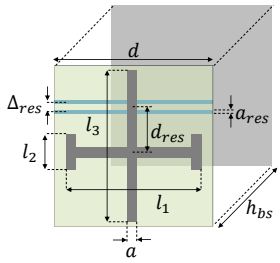


(b)

Fig. 5. The unit cell of FSAs including the superconductive layer and their geometrical parameters (a) FSA$_1$. (b) FSA$_2$.

Since the FSA and the resonator lines are separated by an electrically thin membrane, the structures in Fig. 5 are difficult to model using lumped elements because of the coupling between the layers via higher order Floquet modes. Therefore, an equivalent circuit model based on an admittance matrix, $\bar{Y}_{abs}\left(\vec{k}_\rho\right)$, representing the scattering of the FSA unit cells [15] will be used in the next sections to evaluate the coupling of the FSA KIBs to the optical system. Such matrix was evaluated using CST MWS simulations with periodic boundary conditions.

## III. DUAL BAND FOCAL PLANE ARRAY

In this section, the design of the KIBs based FPA for dual band operation is presented. The distribution of the FSA based KIBs over the focal plane is defined as a trade-off between the expected imager sensitivity, the half power beam-width (HPBW), the mechanical requirements and the fabrication constrains of the detector.

### A. Focal Plane Configuration

The sensitivity of the imager can be estimated as its noise equivalent temperature difference (NETD), which determines the ability of the system in detecting variations in the temperature of the source. The expression of NETD for the absorbers in the focal plane can be expressed as [23]

$$NETD = \frac{1}{\sqrt{2\tau_i^p}} \frac{NEP}{\partial P_{DS}/\partial T} \tag{1}$$

where $P_{DS}$ is the power received by the imager from a distributed incoherent source in two polarizations, NEP is the noise equivalent power of the detectors, and $\tau_i^p$ is integration time per pixel. The NEP of bolometers, such as the KIBs considered in this work, follows the classical phonon noise expression as given in [9].

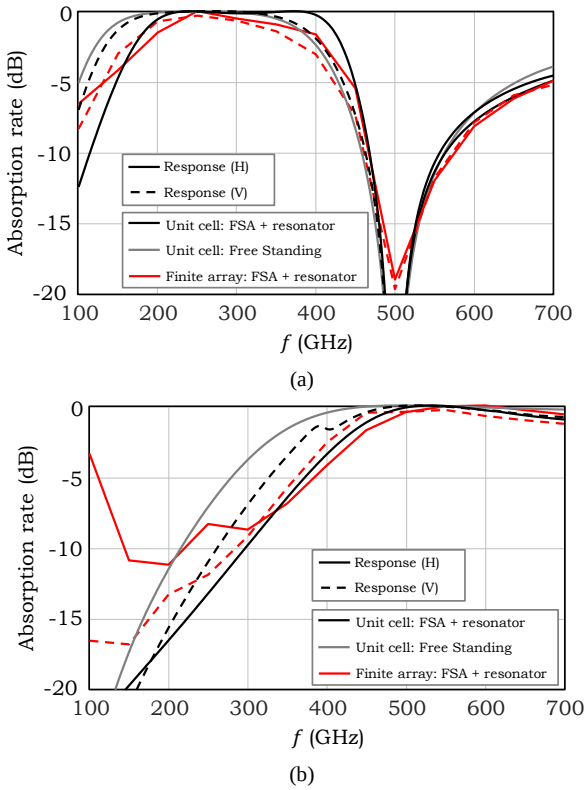


Fig. 6. The absorption rate, simulated with CST MWS, of the optimized design including the resonator layer compared to the free-standing design: (a) $FSA_1$, (b) $FSA_2$. The response for the horizontal and vertical polarizations are referred to as H and V, respectively.

In a fully sampled FPA, the integration time is inversely proportional to the frame rate $\tau_i^p = 1/f_r$. Here, instead, the available detectors on the focal plane are divided between the two bands of interest and a linear scanner is needed to generate fully sampled images. Therefore, the integration time per pixel in (1), $\tau_i^p = \frac{1}{f_r N_s}$, is reduced by the scanning penalty ratio, $N_s$, which in turn leads to a sensitivity degradation. This penalty can be compensated by increasing the power received by the detectors with a larger physical area and more bandwidth.

For non-fully sampled FPAs, the optimum configuration in terms of sensitivity typically leads to a distribution of the detectors over a hexagonal grid combined with a two-dimensional jiggling mechanism, [24], [25], since this allows for the largest physical dimensions of the detectors. However, a FPA based on bare absorbers suffers from a significant penalty in angular resolution for large dimensions as described in [15]. Moreover, a two-dimensional jiggling mechanism requires a scanner operating at much higher speed than the frame rate [24]. Instead, here, the FPA configuration has been designed to be compatible with a single axis scanning mechanism. The proposed focal plane array is a sparse two-dimensional array of detectors placed in a hexagonal grid. This configuration is combined with a one-dimensional mechanical scanner to fully fill the field of view. The layout of a portion of the FPA is shown in Fig. 7(a). Moreover, the arrow shown in the figure indicates the direction of the scanning mechanism.

A passive image requires a sampling of the focal plane field at $0.5\lambda_0 f_\#$ [25], when a square grid FPA is considered. Instead, in the current design, a 45° grid FPA is used, allowing the spacing between the FPA elements to be enlarged to $0.61\lambda_0 f_\#$ [24]. Since the number of sampling points is frequency dependent, the number of $FSA_2$ detectors will be twice the number of $FSA_1$ detectors. The location of the lower bandwidth detectors is shown in Fig. 7(b) with filled black circles. They are located in linear vertical arrays with a spacing of approximately 2 mm and the horizontal distance between them is 6.2 mm. The mechanical scanner will operate in the 45° plane and will acquire $N_{S,1} = 6$ image pixels (non-filled circles in Fig. 7(b)) per detector. The detectors at the higher band are instead distributed in interleaved tilted arrays as shown in Fig. 7(c). As a result, the scanning time penalty will be $N_{S,2} = 12$. This layout has been chosen for three reasons: i) to maximize the physical area for the higher frequency pixels, ii) to use the same scanning mechanism for both frequencies, and iii) to optimize the silicon wafer use, considering the fabrication tolerances. The physical dimensions of the two detector sets are fixed to $w_1 = 0.625\lambda_1 f_\#$ and $w_2 = 0.75\lambda_2 f_\#$, respectively. These values lead to a comparable utilization of the optical aperture to the one of an antenna based FPA [15].

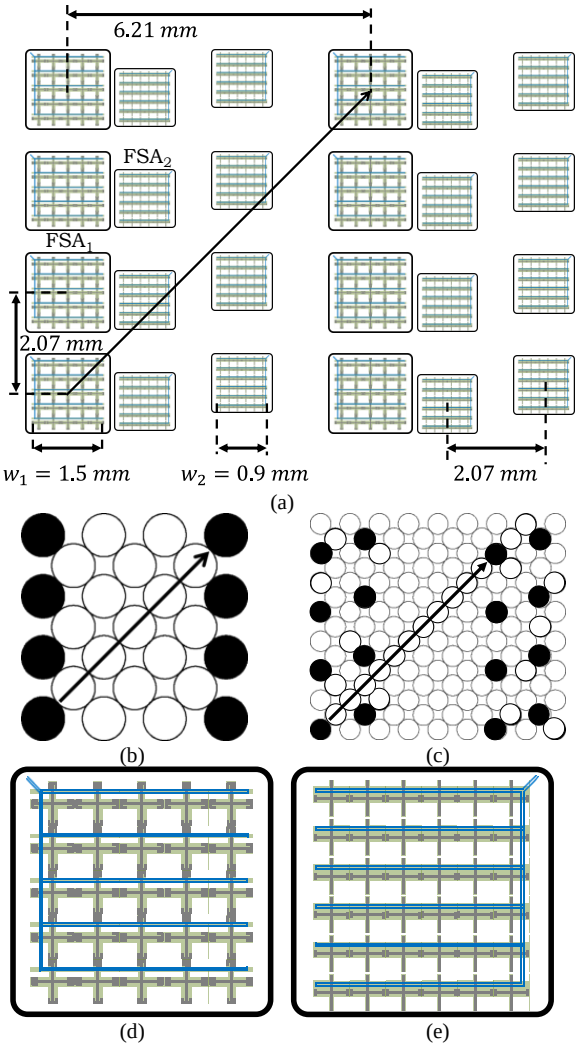


Fig. 7. (a) A portion of the dual band FPA. The arrow indicates the direction of the axis of the mechanical scanner. Schematic representation of the FPA configuration including the position of the actual detectors (black) and the scanned pixels (white) for (b) $FSA_1$. (c) $FSA_2$. The arrow indicates the scanning direction. Detector layouts are shown (d) for $FSA_1$ and (e) for $FSA_2$.

### B. *Detector Layout*

Once the FPA configuration is fixed and the resonator lines are designed, the layout of the detectors can be defined, $FSA_1$ and $FSA_2$ sets consist of arrays of 5x5, Fig. 7(d), and 6x6 elements, Fig. 7(e), respectively. The layout of the FPA and a micrographic photo of the two FSA sets are shown in Fig. 1(a) and (b), respectively. Because of the fabrication process, the cross-section of the detectors will be as schematically reported in Fig. 8.

The response of the finite FSA arrays with the actual fabricated ground plane dimensions and with finite resonator lines was evaluated using CST MWS. The corresponding results are shown in Fig. 5, red curves. The finite and relatively small ground plane, affects the rejection null of the higher band for $FSA_1$ (see Fig. 5(a)). Instead, the actual size of the resonator of $FSA_2$ is responsible of the appearance of a resonant behavior at low frequencies (see Fig. 5(b)). The reason is that the length of the resonators is approximately half wavelength at 190 GHz. As expected, since the resonators are placed horizontally, the resonance is only visible in the horizontal polarization. As discussed in the next section, the effect of this unwanted behavior on the imager performance is negligible.

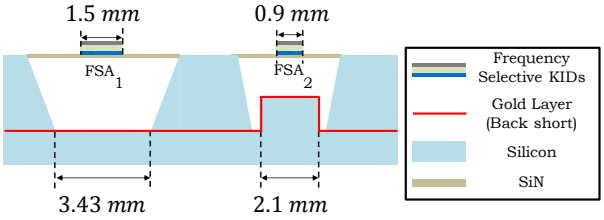


Fig. 8. The cross-section view of the two sets of FSA KIBs.

## IV. Measured Performance

In this section, the experimental performance of the imager in terms of point spread function, effective PSF, and sensitivity is reported. The quasi-optical system of the imager consists of an inversely magnified dual-lens structure as shown in Fig. 9 and described in [14]. In order to limit the absorption of out-of-band radiation, two low-pass filter windows are placed in the optical path between the lenses and the FPA. The upper frequency limit of filter 1 and 2 (-3 dB frequency response), are 684GHz and 1000GHz, respectively. Since the thickness of these filters are small in terms of the wavelength, the insertion loss of the two filter stages are negligible.

The imager performance is first estimated using the spectral analysis technique presented in [15]. In the analysis, the implemented FSA KIBs (Fig. 5) are modeled as an admittance matrix, $\bar{Y}_{abs}(\vec{k}_\rho)$, computed using CST MWS [19], and linked to the spectrum of the optical system (estimated here via physical optics simulations). The differences with the procedure described in [15] and the current configuration are detailed in the Appendix. The effective point spread function of the imaging system is then compared to the measurement results. The sensitivity of the system is also evaluated theoretically at the end of the section using the response to a distributed incoherent source.

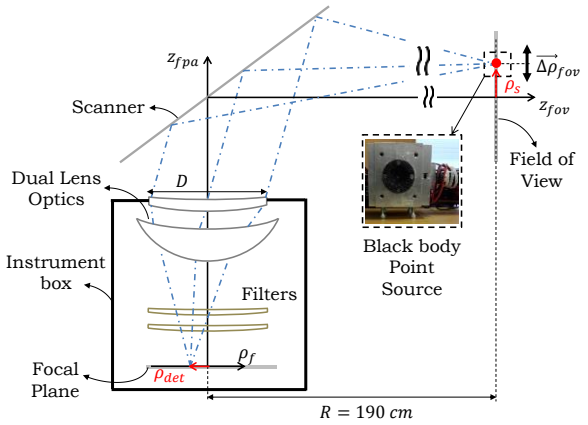


Fig. 9. Schematic representation of the imaging system, including the dual lens optics and the low-pass filter stages. The point source is placed at $\vec{\rho}_s$ in the FoV which corresponds to a specific detector placed at $\vec{\rho}_{det}$ in the focal plane. Arbitrary positions in the FPA are described by the vector $\vec{\rho}_f$.

### A. *Monochromatic Point-Source Response*

In this sub-section, the response of the imager to a monochromatic point source is evaluated for two detectors (one per each frequency band) located at a distance of $\rho_{det} = 31$ mm from the center of the FPA. These locations corresponding to pixels in the field of view (FoV) located 25.82 cm away from the center of the image plane ($\rho_s$ in Fig. 9). This particular configuration is the same one used in the measurements (see Sec. IV.B).

By using the methodology described in [15], one can obtain the spatial fields representing the response of the absorbers to the optical system, $[\vec{e}_t(\vec{\rho}_f\ ,\vec{\rho}_s),\ \vec{h}_t(\vec{\rho}_f\ ,\vec{\rho}_s)]$. By integrating these fields, it is possible to calculate the power received by the imager as a function of the source position as given in (A1). By normalizing the power received at broadside by Poynting vector incident on the optical aperture, we can derive the effective area of the imager, (A2), and from that, the aperture efficiency as (A3). The aperture efficiencies for the two detectors are shown in Fig. 10. The maximum efficiency is approximately 20% in both bandwidths and the results for the two polarizations are comparable. This aperture efficiency includes the spillover associated to the diffracted fields in the focal plane, the ohmic and reflection losses of the dual-lens, the response of the two filter stages, and the frequency response of the FSAs. Moreover, a full wave simulation, similar to the one described in [15], is performed to validate this efficiency. Specifically, GRASP simulation software [22] was used to obtain the direct field generated by the optical system above the detector plane. This direct field is then used as the source in CST MSW to obtain the power dissipated in the absorbers similar to [15]. The efficiency obtained using the full wave simulation is also reported in Fig. 10. As mentioned in Sec. III.B, the resonant behavior at low frequencies found in the finite simulations for the horizontal polarization in $FSA_2$ does not significantly affect the aperture efficiency. The reason is that the absorbed power in the lower portion of the band is dominated by a very low spillover efficiency.

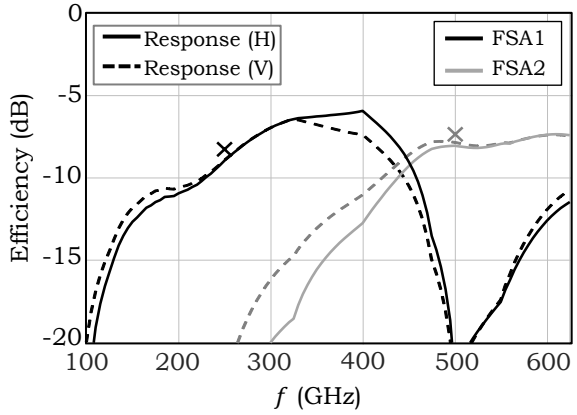


Fig. 10. The aperture efficiency of the two FSA sets ($FSA_1$ with side length 1.5 $mm$ and $FSA_2$ with side length 0.9 $mm$). The cross marks represent the results obtained using the full wave simulations for horizontal polarization.

The point spread function (PSF) of the imager represents the received power as a function of the position of the point source in the FoV, $\vec{\rho}_s + \overrightarrow{\Delta\rho}_{fov}$, Fig. 9. The PSF is calculated as described in the Appendix, (A4) and (A5), for both FSA sets over the operational frequency band, 100 to 625 GHz. In Fig. 11, the two-dimensional PSF of both FSA sets is shown for several frequency points. It can be noticed that the received power outside the specific bandwidth of the two FSAs is low, confirming the predicted rejection. As described in [15], the PSF of an absorber-based imaging system widens rapidly as the absorber dimension enlarges. This effect can be seen by comparing the PSF of $FSA_2$ at 500 GHz with the one at 625 GHz. Moreover, the maximum power received by $FSA_1$ at 500 GHz is about 10 dB lower than the one received at 250 GHz. This result is agreement with the aperture efficiencies shown in Fig. 10. The one-dimensional cut of the PSFs are shown in Fig. 12 at 250 GHz and 500 GHz for $FSA_1$ and $FSA_2$, respectively. Since the PSF for both polarizations are similar, only the results for the vertical polarization are reported here. The PSF obtained using the full wave simulations (GRASP+CST) is also reported in the figure showing very good agreement.

### B. *Incoherent Point-Source Response*

In the previous sub-section, the aperture efficiency and PSF were calculated per frequency points assuming monochromatic point sources. In the following, the response of the imager to an incoherent point source, radiating over the whole frequency band ($BW = 100$ to 625 GHz), is evaluated. The quality of an image is indeed dictated by the power received over the whole bandwidth. This power, in the Rayleigh Jean's limit, for a small source with an average temperature of $T_s$, can be expressed as [26]:

$$P_{DS}^{VP/HP}(\Delta\Omega_{fov}) = \int_{BW} \int_{\Omega_s} \frac{k_B T_s}{\lambda^2} A_{eff}^{VP/HP}(f) F^{VP/HP}\left(f, \Delta\Omega_{fov}\right) d\Omega \, df \qquad (2)$$

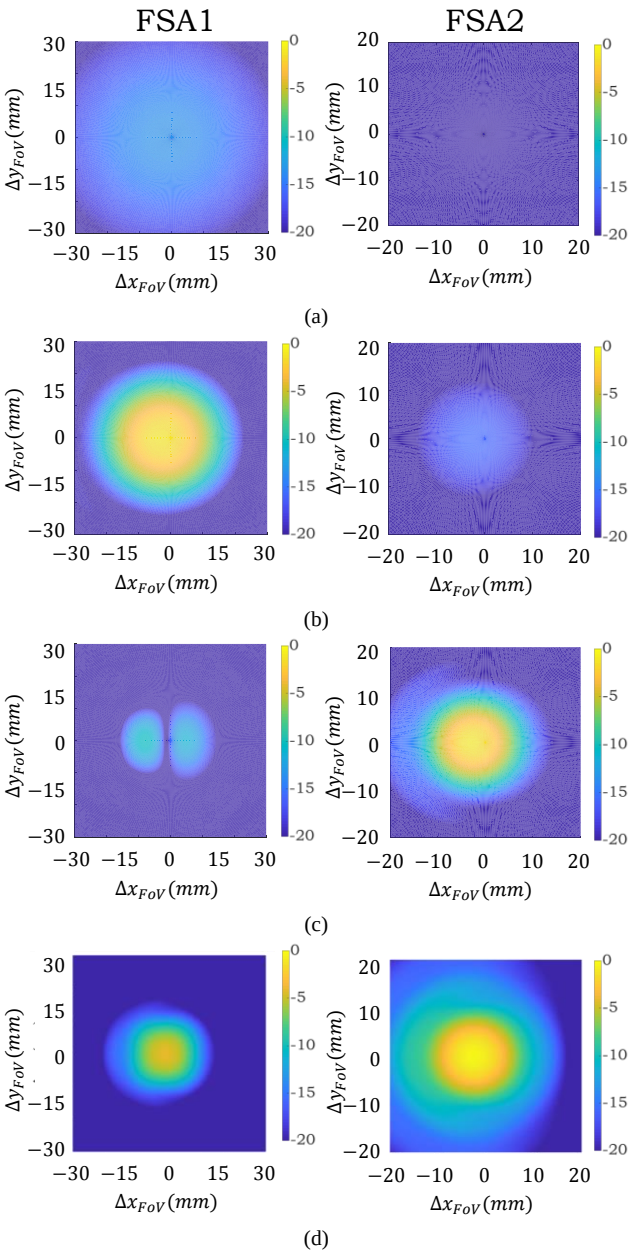


Fig. 11. The 2D PSF of the imager for FSA 1 and 2 at left and right side, respectively, normalized to the maximum value of the function for vertical polarization. At (a) 100 GHz, (b) 250 GHz, (c) 500 GHz and (d) 625 GHz.

where $BW$ represents the bandwidth of the system, the superscripts $VP/HP$ represent, the vertical and horizontal polarizations, respectively, $A_{eff}$ is the effective area of the optical system, $F\left(f, \Delta\Omega_{fov}\right)$ is the point spread function of the optical system (or plane wave response), $\Delta\Omega_{fov}$ corresponds to the angular position of the displaced source with respect to the central position of the source as shown in Fig. A.1. (it can be related to the lateral displacement of the source by $\Delta\Omega_{fov} \simeq \Delta\rho_{fov}/R$, and $\Omega_s$ is the solid angle of the source.

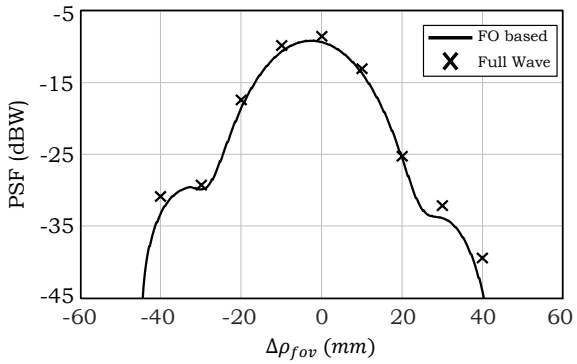


(a)

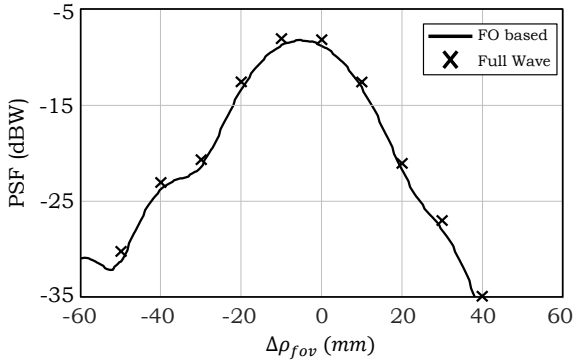


(b)

Fig. 12. The x-cut of the PSF of the imager for both FSAs at the central frequency of their operating band (a) At 250GHz, for $FSA_1$ (b) At 500GHz, for $FSA_2$, for vertical polarization. The cross marks represent the results obtained using the full wave simulations.

For a point source placed at $\vec{\rho}_s + \overrightarrow{\Delta\rho}_{fov}$, the solid angle of the source reduces to $\Delta\Omega_s$, Fig. A1. Therefore, the angular integral in (2) can be simplified to $\Delta\Omega_s$. By normalizing by the term $k_B T_s A_{phy} \Delta\Omega_s$, one can then derive an expression for an *effective point spread function*, similar to what it presented in [23] for single mode antennas, as follows:

$$EF(\Delta\Omega_{fov}) = \int_{BW} \frac{\eta_{ap}(f)}{\lambda^2} F(f, \Delta\Omega_{fov}) df \qquad (3)$$

This effective PSF was measured for two detectors (one per each band) at a distance from the center of the FPA, $\rho_{det} =$ 31 mm using the setup shown in Fig. 9. The black-body point source with the aperture of 2 mm is equivalent to the one used in [8]. The measurement was performed by laterally displacing the black body point source in the FoV. The results are shown in Fig. 13 for both $FSA_1$ and $FSA_2$ and compared to the theoretical computation based on the proposed spectral methodology. The theory and the experiments are in excellent agreement until $-10\ dB$. Below this value, the noise due to the measurement setup is dominant. The pattern shows good symmetry, and its HPBW is reported in Table 3 and compared to the diffraction limited HPBW. The latter can be calculated as the HPBW of an Airy pattern corresponding to the optical aperture ($\simeq$ 16 cm), at the central frequencies of $FSA_1$ and $FSA_2$. The HPBW of the designed imager is comparable to the diffraction limited case.

TABLE 3
ESTIMATED IMAGER PERFORMANCES

| | $FSA_1$ | $FSA_2$ |
|---|---|---|
| $\Delta\rho_{HPBW}^{ave}$ | 1.59 $cm$ | 1.11 $cm$ |
| $\Delta\rho_{HPBW}^{Dif}$ | @ 250 GHz: 2 $cm$ | @ 500 GHz: 1 $cm$ |
| NEP | $2.1 \cdot 10^{-14}\ W/Hz^{1/2}$ | $1.7 \cdot 10^{-14} W/Hz^{1/2}$ |
| NETD | 98 $mK$ | 156 $mK$ |

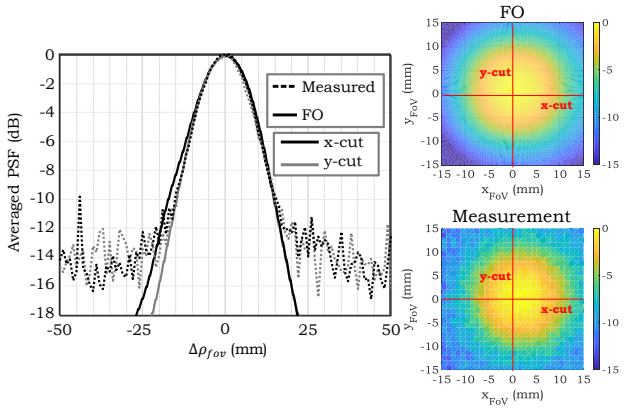


(a)

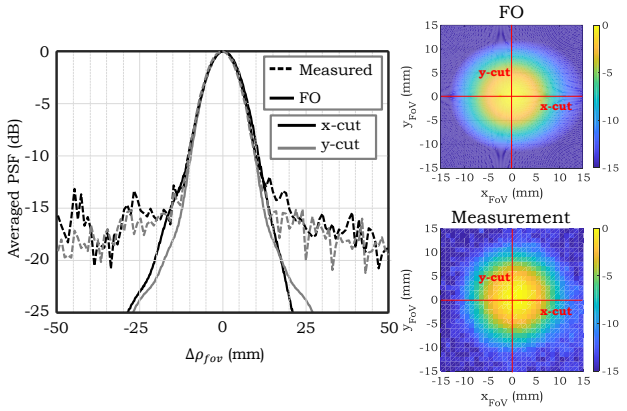


(b)

Fig. 13. The normalized effective point spread function compared between the proposed method and the measurement for (a) $FSA_1$, (b) $FSA_2$ sets, for vertical polarization. The inset indicates the 2D patterns.

## C. Distributed Incoherent Source Response

As shown in [15], the power received by an absorber under an optical system from a distributed source can be expressed as a spectral integral of the effective number of modes as follows:

$$P_{DS}^{VP/HP} = k_B T_s \int_{BW} m_e^{VP/HP}(f) df \qquad (4)$$

where $m_e^{VP/HP}(f) = \eta_{ap}^{VP/HP}(f)/\eta_f^{VP/HP}(f)$ is the effective number of modes. The focusing efficiency, $\eta_f^{VP/HP}(f)$, quantifies how much the imager solid angle enlarges with respect to the diffraction limited case.

For a dual band system, one can represent the power received from the incoherent distributed source as a summation of the in-band and out-band contributions:

TABLE 4
IN AND OUT OF BAND ESTIMATED NORMALIZED THROUGHPUTS

| | $FSA_1$ | $FSA_2$ |
|---|---|---|
| *Operation Band* | $100GHz - 450GHz$ | $450GHz - 625GH$ |
| *Rejection Band* | $450GHz - 625GHz$ | $100GHz - 450GH$ |
| $(m_e)^{in}$ (HP/VP) | 16.8% / 15.7% | 11.5% / 11.8% |
| $(m_e)^{out}$ (HP/VP) | 3.5% / 3.6% | 2.5% / 3.6% |

$$P_{DS}^{VP/HP} = k_B T_s BW_{tot}\left[\left(m_e^{VP/HP}\right)^{in} + \left(m_e^{VP/HP}\right)^{out}\right] \quad (5)$$

where $BW_{tot}$ is the total available bandwidth from 100 GHz to 625 GHz, $(m_e)^{in}$ and $(m_e)^{out}$ are the *in-band* and *out-band* effective number of modes, respectively. These number of modes can be calculated for each FSA sets as:

$$\left(m_e^{VP/HP}\right)^{in} = \frac{1}{BW_{tot}}\int_{BW_{in}} \eta_{ap}^{VP/HP}(f)/\eta_f^{VP/HP}(f)\, df \quad (6)$$

$$\left(m_e^{VP/HP}\right)^{out} = \frac{1}{BW_{tot}}\int_{BW_{out}} \eta_{ap}^{VP/HP}(f)/\eta_f^{VP/HP}(f) df \quad (7)$$

where $BW_{in}$ and $BW_{out}$ are the in-band and out-band operation bandwidths, respectively, of each detector set as defined in Table 4. The same table reports the averaged in-band and out-band effective number of modes for both FSA sets and both horizontal and vertical (H/V) polarizations. The rejection is slightly larger than 1 to 3 (as required) for both FSA sets. The rejection would improve if a multi-layer FSA [18] was integrated in the KIBs.

By considering only the in-band contribution in (5) and using (1), and (4), the sensitivity, NETD, for the pixels associated to each of the bands (including the corresponding scanning penalties discussed in Sec. III.A) has been estimated. The values of sensitivity are reported in Table 3, together with the estimated NEPs measured similarly to the one described in [9]. The reported NETDs are sufficient for security applications. We note that the NETDs are a factor of 3 to 5 lower than those reported from calibrations using an extended blackbody source in [11]. The difference stems predominantly from lower optical losses in the optimized materials, and higher average effective number of modes over the in-band operation bandwidth. We note that a practical demonstration of concealed object detection demonstrating sufficient radiometric contrast in detection is reported in [12].

## V. CONCLUSION

In this contribution, a dual-band focal plane array for security imaging at submillimeter wave frequencies has been presented. The detectors are based on kinetic inductance bolometers, which allow the development of large FPAs at medium cooled temperature. Two FSA sets coupled to superconductive resonator lines were designed to implement a dual color security imager. The geometry of the unit cells is based on a Jerusalem cross configuration and the designed FSAs show a stable angular response and a rejection 1 to 3 of the undesired bandwidth.

The performance of the dual band imager was evaluated using a Fourier optics technique coupled to a Floquet mode analysis. The effective PSF of the imager coupled to a black body point source over a wide frequency band (1:6) was estimated and successfully validated experimentally. The NETD of the imaging system is estimated to be below 200 mK for both frequency bands, and the HPBW of the effective pattern is comparable to the one of a diffraction limited quasi-optical system.

## APPENDIX

In [15], a methodology to evaluate the power received by a distributed absorber under a parabolic reflector was presented. Here this methodology is applied to the combination of the proposed FSA KIBs and near field imaging optics described in [14]. In order to use the spectral analysis tool presented in [15] for this geometry, the plane wave spectrum of the dual lens optics is evaluated using the commercial software GRASP [22]. The dual-lens optics, without including the filter stages, was simulated with a monochromatic point source placed at the position of $\vec{\rho}_s$, see Fig. 9, in the image plane. This location is chosen to be coincident with the maximum field at the location of the detector, $\vec{\rho}_{det}$, for which the measurement is performed: i.e. $\vec{\rho}_s = M\vec{\rho}_{det}$ with $M$ being the optical magnification.

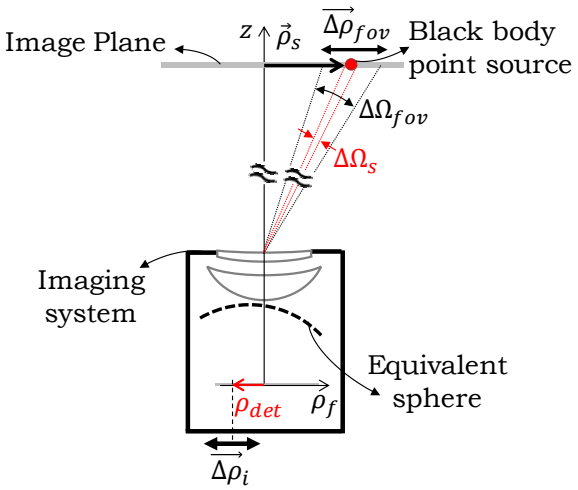


Fig. A1. A simplified schematic of the imaging system illuminated by a black body point source located at $\vec{\rho}_s + \overrightarrow{\Delta\rho_{fov}}$.

The field transmitted by the dual lens was then evaluated via GRASP simulations over an equivalent Fourier optics sphere [15] centered at the detector position, $\vec{\rho}_{det}$, Fig. A.1. By substituting these fields as the geometrical optics fields, $\vec{E}^{GO}(\vec{k}_\rho, \vec{\rho}_s)$, in equation (3) of [15], one can follow the same steps to obtain the spatial fields representing the response of the absorber to the optical system, $\vec{e}^t(\vec{\rho}_f, \vec{\rho}_s)$ and $\vec{h}^t(\vec{\rho}_f, \vec{\rho}_s)$, where the position of the source is explicitly indicated by $\vec{\rho}_s$. Finally, the power absorbed by the FSA KIBs is evaluated as:

$$P_{abs}(f, \vec{\rho}_s) \simeq \frac{1}{2} Re\left\{\iint_{-w/2}^{w/2}\left[\vec{e}_t(\vec{\rho}_f\ , \vec{\rho}_s) \times \vec{h}_t^*(\vec{\rho}_f\ , \vec{\rho}_s)\right] \cdot \hat{z} d\vec{\rho}\right\} \quad (A1)$$

where $w$ is the side length of the FSA.

The effective area of the optical system can be evaluated directly from the power absorbed from the source location, $P_{abs}(f, \vec{\rho}_s)$. The effective area relates to the amplitude of the

active Poynting vector of the source, $|S_{in}(\vec{\rho}_s)|$, at the aperture of the optical system as:

$$A_{eff}(f) = \frac{P_{abs}(f,\vec{\rho}_s)}{|S_{in}(\vec{\rho}_s)|} \quad \text{(A2)}$$

Note this definition applies when the amplitude of the point source over the aperture is uniform. We can define an aperture efficiency, $\eta_{ap}(f)$, related to (A2) by dividing by the physical area of the optical system, $A_{ph}$. In the measurement setup, there are two filter stages which are not simulated in GRASP. Therefore, the aperture efficiency is approximated by:

$$\eta_{ap}(f) \simeq \eta^1_{filt}(f)\eta^2_{filt}(f)\frac{P_{abs}(f,\vec{\rho}_s)}{|S_{in}(\vec{\rho}_s)|A_{ph}} \quad \text{(A3)}$$

where, $\eta^1_{filt}$ and $\eta^2_{filt}$ are the frequency response of the two filter stages.

In order to derive the PSF of the detectors centered at the source location, $\vec{\rho}_s$, we can use the following approximation, (described also in [15]), valid only for small displacements, $\overrightarrow{\Delta\rho}_{fov}$ (see Fig. 9), as follows:

$$P_{abs}\left(f,\vec{\rho}_s + \overrightarrow{\Delta\rho}_{fov}\right) \simeq \frac{1}{2}$$
$$Re\left\{\iint_{-w/2}^{w/2}\left[\vec{e}_t\left(\vec{\rho}_f - \overrightarrow{\Delta\rho}_i, \vec{\rho}_s\right) \times \vec{h}_t^*\left(\vec{\rho}_f - \overrightarrow{\Delta\rho}_i, \vec{\rho}_s\right)\right] \cdot \hat{z}d\vec{\rho}\right\} \quad \text{(A4)}$$

where $\vec{e}_t\left(\vec{\rho}_f - \overrightarrow{\Delta\rho}_i, \vec{\rho}_s\right)$ and $\vec{h}_t\left(\vec{\rho}_f - \overrightarrow{\Delta\rho}_i, \vec{\rho}_s\right)$ are the spatial fields translated by $\overrightarrow{\Delta\rho}_i = -\overrightarrow{\Delta\rho}_{fov}/M$ (Fig. A1).The point spread function can then be expressed as follows:

$$F\left(f, \Delta\Omega_{fov}\right) = \frac{P_{abs}\left(f,\vec{\rho}_s + \overrightarrow{\Delta\rho}_{fov}\right)}{P_{abs}(f,\vec{\rho}_s)} \quad \text{(A5)}$$

where $\Delta\Omega_{fov}$ corresponds to the angular position of the displaced source as shown in Fig. A.1.

## ACKNOWLEDGEMENT

This work was supported by ERC Starting Grant (ERC-2014-StG LAA-THz-CC), No. 639749 and FP7-Security project CONSORTIS. The project also received funding from the Academy of Finland (grant 314447). The authors would like to thank the Netherlands Institute for Space Research (SRON) and Stephen Yates, for offering their black body point source which was used to perform the PSF measurements of this work.

## REFERENCES

[1] R. Appleby and H. Wallace, "Standoff detection of weapons and contraband in the 100 GHz to 1 THz region," *IEEE Trans. on Antennas and Propag.*, vol. 55, no. 11, pp. 2944–2956, Nov. 2007.

[2] E. Grossman, C. Dietlein, J. Ala-Laurinaho, M. Leivo, L. Gronberg, M. Gronholm, P. Lappalainen, A. Rautiainen, A. Tamminen, and A. Luukanen, "Passive terahertz camera for standoff security screening," *Appl. Opt.*, vol. 49, pp. E106–E120, Jul. 2010.

[3] K. B. Cooper, R. J. Dengler, N. Llombart, B. Thomas, G. Chattopadhyay and P. H. Siegel, "THz imaging radar for stand-off personnel screening," in *IEEE Trans. on THz Sci. and Technol.*, vol. 1, no. 1, pp. 169–182, Sept. 2011.

[4] E. Heinz, T. May, D. Born, G. Zieger, K. Peiselt, V. Zakosarenko, T. Krause, A. Krüger, M. Schulz, F. Bauer, and H.-G. Meyer, "Progress in passive submillimeter-wave video imaging," *Proc. SPIE*, June 2014.

[5] S. Rowe, E. Pascale, S. Doyle, C. Dunscombe, P. Hargrave, A. Papageorgio, K. Wood, P. A. R. Ade, P. Barry, A. Bideaud, T. Brien, C. Dodd, W. Grainger, J. House, P. Mauskopf, P. Moseley, L. Spencer, R. Sudiwala, C. Tucker, and I. Walker, "A passive terahertz video camera based on lumped element kinetic inductance detectors," *Rev. of Sci. Inst.*, vol. 87, no. 3, Mar. 2016.

[6] A. Luukanen, T. Kiuru, M.M. Leivo, A. Rautiainen, and J. Varis, "Passive three-colour submillimetre-wave video camera," *Proc. SPIE*, vol. 8715, May 2013.

[7] P. K Day, H. G LeDuc, B. A Mazin, A Vayonakis, J. Zmuidzinas, "A broadband superconducting detector suitable for use in large arrays," *Nature*, vol. 425, pp. 817–821, Oct. 2003.

[8] J. J. A Baselmans, J. Bueno, S. J. C. Yates, O. Yurduseven, N. Llombart, K. Karatsu, A. M. Baryshev, L. Ferrari, A. Endo, D. J. Thoen, P. J. de Visser, R. M. J. Janssen, V. Murugesan, E. F. C. Driessen, G. Coiffard, J. Martin-Pintado, P. Hargrave, and M. Griffin, "A kilo-pixel imaging system for future space based far-infrared observatories using microwave kinetic inductance detectors," *Astron. and & Astrphys. ArXiv e-prints*, vol. 601, Sept. 2016.

[9] A. V. Timofeev, V. Vesterinen, P. Helist, L. Grnberg, J. Hassel, and A. Luukanen, "Submillimeter-wave kinetic inductance bolometers on free-standing nanomembranes," *Superconductor Sci. and Technol.*, vol. 27, no. 2, Dec. 2013.

[10] S. Doyle, P. Mauskopf, J. Naylon, A. Porch, and C. Duncombe, "Lumped element kinetic inductance detectors," *J. of Low Temp. Phys.*, vol. 151, no. 1, pp. 530–536, Jan. 2008.

[11] A. Timofeev, J. Luomahaara, L. Grönberg, A. Mäyrä, H. Sipola, M. Aikio, M. Metso, V. Vesterinen, K. Tappura, J. Ala-Laurinaho, A. Luukanen, and J. Hassel, "Optical and electrical characterization of a large kinetic inductance bolometer focal plane array," *IEEE Trans. on THz Sci. and Technol.*, vol. 7, no. 2, pp. 218–224, Mar. 2017.

[12] J. Hassel, S. O. Dabironezare, E. Gandini, L. Grönberg, H. Sipola, A. Rautiainen, A. Tamminen, M. Leivo, H. Lindström, H. Vasama, A. Luukanen, and N. Llombart, "Dual-band submillimeter-wave kinetic inductance bolometers and an imaging system for contraband object detection," *Proc. SPIE*, vol. 10634, pp. 10634F1-6, May 2018.

[13] F. Costa, A. Kazemzadeh, S. Genovesi, A. Monorchio, "Electromagnetic absorbers based on frequency selective surfaces," *FERMAT*, Jan. 2013.

[14] E. Gandini, A. Tamminen, A. Luukanen, and N. Llombart, "Wide field of view inversely magnified dual-lens for near-field sub-millimeter wavelength imagers," *IEEE Trans. on Antennas Propag.*, vol. 66, no. 2, pp. 541–549, Nov. 2017.

[15] N. Llombart, S.O. Dabironezare, G. Carluccio, A. Freni, and A. Neto, "Reception power pattern of distributed absorbers in focal plane arrays: a Fourier Optics analysis," *IEEE Trans. on Antennas Propag.*, awaiting publication.

[16] D.C. Mattis, and J. Bardeen, "Theory of the anomalous skin effect in normal and superconducting metals," *Phys. Rev.*, vol. 111, no. 2, pp. 412–417, Jul. 1958.

[17] B. Blázquez, N. Llombart, D. Cavallo, A. Freni, and A. Neto, "A rigorous equivalent network for linearly polarized THz absorbers," *IEEE Trans. on Antennas and Propag.*, vol. 62, no. 10, pp. 5077–5088, Oct. 2014.

[18] B. Munk, *Frequency Selective Surfaces Theory and Design*, Wiley-Interscience, 2000.

[19] *CST Microwave StudioVersion 2014.00*, Comput. Simul. Technol. AG, Darmstadt, Germany, 2014.

[20] G. I. Kiani, K. L. Ford, K. P. Esselle, A. R. Weily, and C. J. Panagamuwa, "Oblique incidence performance of a novel frequency selective surface absorber," *IEEE Trans. on Antennas and Propag.*, vol. 55, no. 10, pp. 2931–2934, Oct. 2007.

[21] K. Zhang, W. Jiang, and S. Gong, "Design bandpass frequency selective surface absorber using LC resonators," *IEEE Antennas and Wirel. Propag. Lett.*, vol. 16, pp. 2586–2589, Aug. 2017.

[22] *GRASP Version 10.5.0*, TICRA, Copenhagen, Denmark, 2015.

[23] S. L. van Berkel, O. Yurduseven, A. Freni, A. Neto, and N. Llombart, "THz imaging using uncooled wideband direct detection focal plane arrays," *IEEE Trans. on THz Sci. and Technol.*, vol. 7, no. 5, pp. 481–492, Sept. 2017.

[24] S. Rao, L. Shafai, and S. K. Sharma, eds., *Handbook of Reflector Antennas and Feed Systems Volume III: Applications of Reflectors*, Artech House, 2013.

[25] M. J. Griffin, J. J. Bock, and W. K. Gear, "Relative performance of filled and feedhorn-coupled focal-plane architectures," *Appl. Opt*., vol. 41, no. 31, pp. 6543–6554, Nov. 2002.
[26] David Long, Fawwaz T. Ulaby, *Microwave Radar and Radiometric Remote Sensing*, Artech House, Chapter 6, 2015.

**Shahab Oddin Dabironezare** (S'11) received the B.Sc. degrees (*cum laude*) from Ferdowsi University of Mashhad (FUM), and M.Sc. degree from the Delft University of Technology (TU Delft), in electrical engineering in 2013 and 2015, respectively. He is currently pursuing the Ph.D. degree in Terahertz Sensing Group, TU Delft.

His research interests include quasi-optical systems, analytical/numerical techniques in electromagnetics, passive imaging systems, and wideband antenna designs for millimeter and submillimeter-wave applications.

**Juha Hassel** received the M.Sc (Tech) and D.Sc. (Tech) degrees in engineering physics from the Helsinki University of Technology (currently Aalto University), Espoo, Finland, in 1999 and 2004, respectively.

He has worked at the VTT Technical Research Centre of Finland, as Research Scientist since 1999, as Senior Scientist since 2008, and as Principal Scientist since 2015. From 2001 to 2002, he was a Visiting Researcher with the University of California, Berkeley, CA, USA. Currently he is also the leader of the THz Sensing team within the Academy of Finland Centre of Excellence in Low Temperature Quantum Phenomena and Devices.

His research interests include instrumentation for THz sensing and imaging, and applications of low temperature sensors and electronics.

**Erio Gandini** (M'17) received the M.Sc. degree in electrical engineering from the University of Modena and Reggio Emilia, Modena, Italy, in 2009, and the Ph.D. degree in electrical engineering from the University of Rennes 1, Rennes, France, in 2012.

In 2011, he was a Visiting Ph.D. Student with the University of Michigan, Ann Arbor, MI, USA. In 2013, he joined the Ecole Polytechnique Fédérale de Lausanne, Lausanne, Switzerland. In 2013, he joined the THz Sensing Group, Delft University of Technology, Delft, The Netherlands, where he is currently a Research Scientist. Since 2016, he has been an Antenna Scientist with the Radar Department, TNO Defence, Security and Safety, The Hague, The Netherlands.

His current research interests include applied electromagnetics, quasi-optical systems, phased array antennas, submillimeter and terahertz imaging systems, frequency selective surfaces, and beam-forming networks.

**Leif Grönberg** received the M.Sc. (Tech.) and Lic.Sc. (Tech.) degrees in electrical engineering from the Helsinki University of Technology (currently Aalto University), Espoo, Finland, in 1980 and 1984, respectively.

In 1986, he joined the Superconducting Device Group, VTT, Espoo. He was actively involved in developing the refractory junction technology for VTT SQUIDs. He has been the Principal Investigator of the fabrication technology for SQUID and terahertz systems, the former has been commercialized in MEG systems and the latter in THz cameras for security imaging. He has also been working with process development and fabrication of thin-film devices for various applications. He is currently a Senior Scientist with the Nanoelectronics Team, VTT.

**Nuria Llombart** (S'06–M'07–SM'13) received the Master's degree in electrical engineering and Ph.D. degrees from the Polytechnic University of Valencia, Valencia, Spain, in 2002 and 2006, respectively.

During her Master's degree studies, she spent one year at the Friedrich-Alexander University of Erlangen-Nuremberg, Erlangen, Germany, and worked at the Fraunhofer Institute for Integrated Circuits, Erlangen, Germany. From 2002 to 2007, she was with the Antenna Group, TNO Defense, Security and Safety Institute, The Hague, The Netherlands, working as a Ph.D. student and afterwards as a Researcher. From 2007 to 2010, she was a Postdoctoral Fellow with the California Institute of Technology, working with the Submillimeter Wave Advance Technology Group, Jet Propulsion Laboratory, Pasadena, CA, USA. She was a "Ramón y Cajal" fellow in the Optics Department, Complutense University of Madrid, Madrid, Spain, from 2010 to 2012. In September 2012, she joined the THz Sensing Group, Technical University of Delft, Delft, The Netherlands, where as of February 2018 she is a Full Professor. She has coauthored more than 150 journal and international conference contributions. Her research interests include the analysis and design of planar antennas, periodic structures, reflector antennas, lens antennas, and waveguide structures, with emphasis in the THz range.

Dr. Llombart was the recipient H. A. Wheeler Award for the Best Applications Paper of 2008 in the IEEE TRANSACTIONS ON ANTENNAS AND PROPAGATION, the 2014 THz Science and Technology Best Paper Award of the IEEE Microwave Theory and Techniques Society, and several NASA awards. She was also the recipient of the 2014 IEEE Antenna and Propagation Society Lot Shafai Mid-Career Distinguished Achievement Award. She serves as a Board member of the IRMMW-THz International Society. In 2015, she was the recipient of European Research Council Starting Grant.